

Rational design principles for giant spin Hall effect in *5d*-transition metal oxides

Priyamvada Jadaun,^{1,*} Leonard F Register,¹ and Sanjay K Banerjee¹

¹*Department of Electrical and Computer Engineering,
The University of Texas at Austin, Austin, Texas. USA.*

(Dated: July 29, 2022)

Abstract

Spin Hall effect (SHE) has emerged as a promising contender for the realization of high-density and low-power, next-generation memory. However, most materials explored so far have demonstrated either a spin Hall efficiency or a longitudinal conductivity that is too low for real-world applications. Here, we report the discovery of giant spin Hall efficiencies in *5d*-transition metal oxides (TMOs) that are **at least an order of magnitude** larger than those reported for any TMOs, and greater than those observed for all other measured materials, except for the topological insulators $\text{Bi}_x\text{Se}_{1-x}$ and $\text{Bi}_{1-x}\text{Sb}_x$. Inspired by the vast tunability of properties possible for TMOs, we also present **five general rational design principles** for the generation of giant SHE in TMOs. Our findings bring new insight into the physics driving SHE in TMOs, including the vital role played by **crystal field**, as well as the nuanced role of electron correlation. We report on the potential of **anti-perovskites** for generating giant SHE and facilitating the exploration of multifunctional spin Hall devices.

* priyamvada@utexas.edu

I. INTRODUCTION

Our society's fast growing demand for data storage has created an urgent need for high-density, low-power and high-speed memory technology [1]. The most promising device to realize emergent memory technology is the magnetoresistive random access memory (MRAM) [2], owing to its non-volatility, quick random access and low degradation [3–5]. Control of the magnetic bit in an MRAM via spin torque, which is applied by spin currents, instead of control via magnetic fields, is a more energy-efficient design [6–8]. The emerging area of spin orbitronics [9] utilizes spin orbit coupling (SOC) to efficiently generate spin currents via the spin Hall effect (SHE) [10–15], the Rashba–Edelstein effect [16–18], or the spin-momentum locking in topological insulators [19–21, 32].

While spin orbitronics based emergent memory devices demonstrate significant technological promise, real-world applications still face considerable challenge. In order for an emergent spin orbitronics device to be more energy-efficient than a commercial spin transfer torque device, where spin currents are generated via spin orbit coupling (SOC) in the former and via ferromagnets in the latter, the spin Hall angle (Θ_{SH}) should be greater than 1 [22]. Spin Hall angle (Θ_{SH}) is the ratio of the spin current to the charge current flowing, and it captures the efficiency of conversion of charge current to spin current. Recent years have seen a flurry of research aimed at discovering materials with ever increasing values of Θ_{SH} , ranging from heavy metals, topological insulators to transition metal oxides. The largest values of Θ_{SH} reported for heavy metals were for Pt ($\Theta_{\text{SH}} \sim 0.07$) [25–28], β -W ($\Theta_{\text{SH}} \sim 0.3$) [29] and β -Ta ($\Theta_{\text{SH}} \sim 0.14$) [30], while lanthanides like Dy have demonstrated a $\Theta_{\text{SH}} \sim 0.1$ [31]. Subsequently, giant Θ_{SH} was observed in topological insulators such as Bi_2Se_3 ($\Theta_{\text{SH}} \sim 3$) [32] and $\text{Bi}_x\text{Se}_{1-x}$ ($\Theta_{\text{SH}} = 18.8$) [23]. Recently, colossal SHE ($\Theta_{\text{SH}} \sim 52$) has been theoretically predicted [33] and experimentally observed [22] for the topological insulator $\text{Bi}_{1-x}\text{Sb}_x$. However, these topological insulators, with the exception of $\text{Bi}_{1-x}\text{Sb}_x$, are limited in their applicability due to their low longitudinal conductivity [22]. Of late, the search for giant SHE has turned to transition metal oxides. Large values of Θ_{SH} have been reported for SrIrO_3 with $\Theta_{\text{SH}} \sim 0.5$ [34], and for SrRuO_3 with $\Theta_{\text{SH}} \sim 0.24$ [35], while a low-moderate value of $\Theta_{\text{SH}} \sim 0.04$ has been observed for IrO_2 [24].

In this paper we report the discovery of giant spin Hall angles ($\Theta_{\text{SH}} \sim -2.5$ to 7.4) in $5d$ -transition metal oxides ($5d$ -TMOs) that are **at least an order of magnitude** larger than

those reported for any transition metal oxides (TMOs) so far. Additionally, the Θ_{SH} values seen by us in oxides are greater than those observed for all other measured materials except for the topological insulators $\text{Bi}_x\text{Se}_{1-x}$ and $\text{Bi}_{1-x}\text{Sb}_x$. The estimated longitudinal conductivities for our best materials are $\geq 5 \times 10^2$ S/cm, making them suitable for applications in emergent memory technology [22]. In addition to demonstrating giant spin Hall effect (SHE), TMOs are a unique class of materials as their multiple degrees of freedom, namely, charge, spin, orbital, and lattice, are intertwined with one another [36]. TMOs thus present us with a vast tunable space where we can design materials with structures and chemistry precisely tailored to our technological needs [34, 37]. It is likely that the giant SHE values reported by us in TMOs can be further enhanced by careful engineering. Our work thus opens new possibilities for the development of efficient memory devices that operate on low-power.

Motivated by the inherent tunability of the structure and properties of TMOs, we demonstrate the origin of large SHE in TMOs and deduce **five general rational design principles** for generating giant SHE in TMOs. These are (*C1*) weak crystal fields, (*C2*) structural distortions, (*C3*) optimal positioning of the Fermi level, (*C4*) mixing of $J_{\text{eff}} = 1/2$ & $3/2$ bands and (*C5*) moderate electron correlations, where the label *C* stands for condition. Our design principles can facilitate further improvement of spin Hall values in TMOs and bring **new insight** into the physics driving the spin Hall effect. We uncover the surprisingly vital role played by **crystal field** (*C1*) in determining spin Hall values. An unexpected direct result of this importance of crystal field is that TMOs with an **anti-perovskite** structure show promise towards giant SHE, owing to their weak crystal field (*C1*). The same condition (*C1*) in reverse hinders the SHE in TMOs with a perovskite or pyrochlore type structure, due to the typically large crystal field found in these materials. This finding on perovskites and pyrochlores is surprising given the wide interest in literature on the strong effects of SOC in these materials [38–44]. Another surprising finding reported here is the subtle relationship between electron correlation and spin Hall conductivity (SHC). In contrast to the expectation that moderate electron correlations generally enhance SOC by localizing electrons [45] and should therefore enhance spin Hall conductivity (SHC), we report that the effect of correlations on SHC is more nuanced and depends on band structure details. We also enumerate large values of spin Hall angle, $\Theta_{\text{SH}} \geq 0.2$, for a significant number of materials. Finally, our findings open multiple pathways for future research in multifunctional materials. TMOs in general, including anti-perovskites, have shown a variety of interesting

properties such as magnetism [48, 49], frustrated magnetism [50], ferroelectrics [47] and spin glass state [51]. The promise of giant SHE in anti-perovskites presents an opportunity to merge this SHE with other functional properties of anti-perovskites (or other TMOs) to yield multifunctional devices. Multifunctionality might be possible via elemental substitution or interfacial stacking of thin films. If realized, such work would further the study of interesting physics and could be a major step forward in the development of emergent, ultra-low power memory devices.

II. RESULTS

A. General origin of the spin Hall effect

We now derive the general factors that control the value of spin Hall effect, specifically, the type of spin Hall effect that arises from the intrinsic bandstructure of a material, called the intrinsic spin Hall effect [59, 60]. We start with the expression for spin Hall conductivity (SHC) obtained from linear response theory. Let \hat{H} represent the total Hamiltonian of system and \hat{H}_0 represent the Hamiltonian without SOC ($\lambda \hat{l} \cdot \hat{s}$). Let $\sigma_{\alpha\beta}^{n,s}$ and $\Omega_{\alpha\beta}^{n,s}$ represent the $\alpha\beta$ component of the band (n) resolved SHC and spin Berry curvature, respectively, of this system. The spin momentum is along the direction s , and α, β, s are along the coordinate axes (x, y, z).

$$\hat{H} = \hat{H}_0 + \lambda \hat{l} \cdot \hat{s} \quad (1)$$

$$\sigma_{\alpha\beta}^s = -\frac{e}{\hbar} \int_{BZ} \frac{d\vec{k}}{(2\pi)^3} \sum_n f_n(\vec{k}) \Omega_{\alpha\beta}^{n_{\vec{k}},s} \quad (2)$$

In the above, suppressing the index \vec{k} :

$$\Omega_{\alpha\beta}^{n,s} = -2\text{Im} \left[\sum_{m \neq n} \frac{j_{nm,\alpha}^s v_{mn,\beta}}{(\epsilon_m - \epsilon_n)^2} \right] \quad (3)$$

$$j_{nm,\alpha}^s = \frac{1}{2} \sum_l [\langle n | \hat{s}_s | l \rangle \langle l | \hat{v}_\alpha | m \rangle + \langle n | \hat{v}_\alpha | l \rangle \langle l | \hat{s}_s | m \rangle] \quad (4)$$

$$v_{mn,\beta} = \langle m | \hat{v}_\beta | n \rangle \quad (5)$$

These equations demonstrate that the spin Berry curvature originates from the product of the spin operator (\hat{s}_s) and the anomalous velocity operators ($\hat{v}_\alpha, \hat{v}_\beta$). We assume that the spin conserving part of the SOC operator ($\lambda \hat{l}_z \hat{s}_z$) makes the dominant contribution to the

SHC, as compared to the spin mixing part. We include our justification for this assumption in supplementary material and show that this assumption is often, though not always, valid. Substituting 4 into 3, we obtain:

$$\Omega_{\alpha\beta}^{n,s} = -\text{Im} \sum_{m \neq n, l} \frac{[\langle n | \hat{s}_s | l \rangle \langle l | \hat{v}_\alpha | m \rangle + \langle n | \hat{v}_\alpha | l \rangle \langle l | \hat{s}_s | m \rangle]}{(\epsilon_m - \epsilon_n)^2}. \quad (6)$$

In the spin basis, we can write the time reversed pair of eigenstates $|n_{\vec{k}}\rangle$ and $|n_{-\vec{k}}\rangle$ as:

$$|n_{\vec{k}}\rangle \equiv \begin{bmatrix} \mu_n \\ \nu_n \end{bmatrix} |n_{-\vec{k}}\rangle \equiv \begin{bmatrix} -\nu_n^* \\ \mu_n^* \end{bmatrix} \quad (7)$$

According to our assumption, we neglect any contribution to SHC from the spin mixing parts of SOC. The expression for $\Omega_{\alpha\beta}^{n,s}$ can thus be simplified to include only the anomalous velocity terms that arise from the spin conserving part of the Hamiltonian,

$$\hat{v}_\alpha = \frac{\partial}{\partial k_\alpha} (\hat{H}_0 + \lambda \hat{l}_z \hat{s}_z) = \begin{bmatrix} \hat{v}_\alpha^0 + \hat{v}_\alpha^z & 0 \\ 0 & \hat{v}_\alpha^0 - \hat{v}_\alpha^z \end{bmatrix}, \quad (8)$$

where $\hat{v}_\alpha^0 = \partial/\partial k_\alpha (\hat{H}_0)$ and $\hat{v}_\alpha^z = \partial/\partial k_\alpha (\lambda \hat{l}_z/2)$. If \hat{v}_α and \hat{v}_β cannot mix spin, neither can \hat{s}_s . Thus the non-zero terms in 6 are:

$$\begin{aligned} \langle n_{\vec{k}} | \hat{s}_s | l_{\vec{k}} \rangle &= \langle \mu_n | \mu_l \rangle - \langle \nu_n | \nu_l \rangle \equiv s_{nl}; \langle n_{-\vec{k}} | \hat{s}_s | l_{-\vec{k}} \rangle = \langle \nu_l | \nu_n \rangle - \langle \mu_l | \mu_n \rangle = -s_{nl}^* \\ \langle l_{\vec{k}} | \hat{v}_\alpha | m_{\vec{k}} \rangle &= \langle \mu_l | \hat{v}_\alpha^0 + \hat{v}_\alpha^z | \mu_m \rangle + \langle \nu_l | \hat{v}_\alpha^0 - \hat{v}_\alpha^z | \nu_m \rangle = v_{\alpha,lm}^0 + v_{\alpha,lm}^z \\ \langle l_{-\vec{k}} | \hat{v}_\alpha | m_{-\vec{k}} \rangle &= \langle \mu_l | \hat{v}_\alpha^0 - \hat{v}_\alpha^z | \mu_m \rangle^* + \langle \nu_l | \hat{v}_\alpha^0 + \hat{v}_\alpha^z | \nu_m \rangle^* = (v_{\alpha,lm}^0)^* - (v_{\alpha,lm}^z)^* \\ \text{where : } v_{\alpha,lm}^0 &\equiv \langle \mu_l | \hat{v}_\alpha^0 | \mu_m \rangle + \langle \nu_l | \hat{v}_\alpha^0 | \nu_m \rangle; v_{\alpha,lm}^z \equiv \langle \mu_l | \hat{v}_\alpha^z | \mu_m \rangle - \langle \nu_l | \hat{v}_\alpha^z | \nu_m \rangle. \end{aligned} \quad (9)$$

Substituting α with β , n with m and l with n , we write the complete expression for the spin Berry curvature for the eigenstate $|n_{\vec{k}}\rangle$, i.e., $\Omega_{\alpha\beta}^{n_{\vec{k}},s}$ as:

$$\Omega_{\alpha\beta}^{n_{\vec{k}},s} = -\text{Im} \sum_{m \neq n, l} \frac{[s_{nl}(v_{\alpha,lm}^0 + v_{\alpha,lm}^z) + s_{lm}(v_{\alpha,nl}^0 + v_{\alpha,nl}^z)](v_{\beta,mn}^0 + v_{\beta,mn}^z)}{(\epsilon_m - \epsilon_n)^2}. \quad (10)$$

Similarly, we write the spin Berry curvature for the time reversal partner of $|n_{\vec{k}}\rangle$, which is $|n_{-\vec{k}}\rangle$, i.e., $\Omega_{\alpha\beta}^{n_{-\vec{k}},s}$ as:

$$\Omega_{\alpha\beta}^{n_{-\vec{k}},s} = -\text{Im} \sum_{m \neq n, l} \frac{[-s_{nl}^*(v_{\alpha,lm}^0 - v_{\alpha,lm}^z)^* - s_{lm}^*(v_{\alpha,nl}^0 - v_{\alpha,nl}^z)^*](v_{\beta,mn}^0 - v_{\beta,mn}^z)^*]}{(\epsilon_m - \epsilon_n)^2}. \quad (11)$$

The total SHC of the material would involve adding the spin Berry curvature contributions from both the time reversal partners. Comparing 10 and 11 and using $\text{Im}(A^* B^* C^*) =$

$-\text{Im}(ABC)$, we are left with only two non-zero terms that can contribute to the total SHC ($\sigma_{\alpha\beta}^s$). The first term is $(s_{nl}v_{\alpha,lm}^z v_{\beta,mn}^z + s_{lm}v_{\alpha,nl}^z v_{\beta,mn}^z)$. This term arises from the anomalous velocity originating in the rotation of eigenstates, or in other words, in the mixing of orbitals, caused by the spin conserving part of SOC. The second term $(s_{nl}v_{\alpha,lm}^0 v_{\beta,mn}^0 + s_{lm}v_{\alpha,nl}^0 v_{\beta,mn}^0)$ arises from the anomalous velocity originating in the rotation of eigenstates caused by the spin independent part of the Hamiltonian (\hat{H}_0). For materials with inversion and time reversal symmetry, which includes all materials in this study, the second term which is related to the Berry curvature, is zero [61].

In the basis of the d orbitals of TMOs, \hat{l}_z mixes either d_{xz} with d_{yz} orbitals or it mixes d_{xy} with $d_{x^2-y^2}$ orbitals. Consequently, for $\hat{v}_\alpha^z = \partial/\partial k_\alpha(\lambda\hat{l}_z/2)$, the only non-zero components of \hat{v}_α^z arise either from the mixing of d_{xz} with d_{yz} orbitals or the mixing of d_{xy} with $d_{x^2-y^2}$ orbitals. From the derivation above we deduce the general rules for obtaining significant spin Hall effect in materials with inversion and time reversal symmetry, as enumerated below.

R1. Firstly, non-zero SHE requires the bands of character d_i and d_j to be close enough in energy at a given \vec{k} , such that the SOC can mix these states, where $i = xz, j = yz$, or, $i = xy, j = x^2 - y^2$ for d orbitals.

R2. Secondly, for non-zero SHC, the Fermi level should pass through the region where the bands d_i and d_j are crossing or being mixed by SOC. If the Fermi level does not pass through the band mixing region, all interacting states will have the same occupation. As a result, $f_n(\vec{k})v_{\alpha,nm}^z v_{\beta,mn}^z$ will exactly cancel with $f_n(\vec{k})v_{\alpha,mn}^z v_{\beta,nm}^z$ as $l_{z,mn} = l_{z,nm}^*$. Thus, the Fermi level positioning is critical to the total value of SHC.

R3. Thirdly, the coupling of states via SOC will contribute to spin Berry curvature only if there are net transitions between d_i and d_j .

B. Rational design principles for large SHE in TMOs

In the section above we have derived three basic rules that govern the value of SHC in d orbital materials. From these we will now deduce the rational design principles for large SHC in TMOs. The band structure of a transition metal oxide is generally explained with the help of crystal field theory (CFT) [62, 63]. Crystal field theory considers a transition metal atom with its detailed electronic structure in an environment of ligands that are considered structure-less. The primary effect of the ligands is to alter the electronic structure of the

transition metal due to repulsion between the transition metal electrons and the electronegative ligand ions. The repulsive ligand field, and consequently the electronic structure, is determined by the geometry of the ligands surrounding the transition metal. For instance, in most TMOs considered here, the transition metal is surrounded by six oxygen atoms that form an octahedra, resulting in what is called an octahedral crystal field (see Fig. 1). For an octahedral crystal field, amongst the $5d$ orbitals of the transition metal, $d_{x^2-y^2}$ and d_{z^2} orbitals point in the direction of the ligands and experience strong repulsion. These orbitals are thus pushed higher in energy in the bandstructure and together constitute what is called the e_g manifold. On the other hand, the d_{xz} , d_{yz} and d_{xy} orbitals point away from the repulsive ligands, thereby experiencing lower repulsion and lying lower in energy in the bandstructure. These latter three orbitals constitute the t_{2g} manifold. The concerted effect of an octahedral crystal field on the electronic structure is to split the otherwise degenerate $5d$ -bands of the transition metal into a lower energy three-fold degenerate t_{2g} and an higher energy two-fold degenerate e_g (see Fig. 1). In contrast, a cubic crystal field comprises of a transition metal surrounded by eight ligand ions arranged at the corners of a cube. This cubic field splits the transition metal $5d$ -bands into an inverse, lower energy e_g and a higher energy t_{2g} manifold.

Putting together CFT with the general rules (R) controlling the value of SHC that we had derived before, we will now deduce our five rational design principles to obtain large SHE. In general, Berry curvature results from a rotation of a degree of freedom (DOF) of the electronic wavefunction with a periodic variation of some parameter [61]. For SHE, which derives from spin Berry curvature, the degree of freedom is the orbital angular momentum (l) and the parameter is the wavevector (\vec{k}). For d -orbitals there are five possible DOFs. However in TMOs, the crystal field splits this space into smaller subspaces spanned by fewer DOFs. For instance, in octahedral and cubic fields the d -bands are split into an e_g (DOF=2) and a t_{2g} (DOF=3) manifold. The splitting of the larger manifold into these smaller spaces reduces the possibilities for rotation of DOFs thereby reducing the possible spin Berry curvature and consequently reducing SHE. Therefore, we reason that large values of SHE are encouraged by **weak crystal fields**. This is **condition 1 (C1)**. Specifically for TMOs, we have shown above that there are two possible contributions to SHE, one that arises from the mixing of d_{xz} and d_{yz} orbitals, and another that arises from the mixing of d_{xy} and $d_{x^2-y^2}$ orbitals. It follows that SHE is maximized when both these contributions

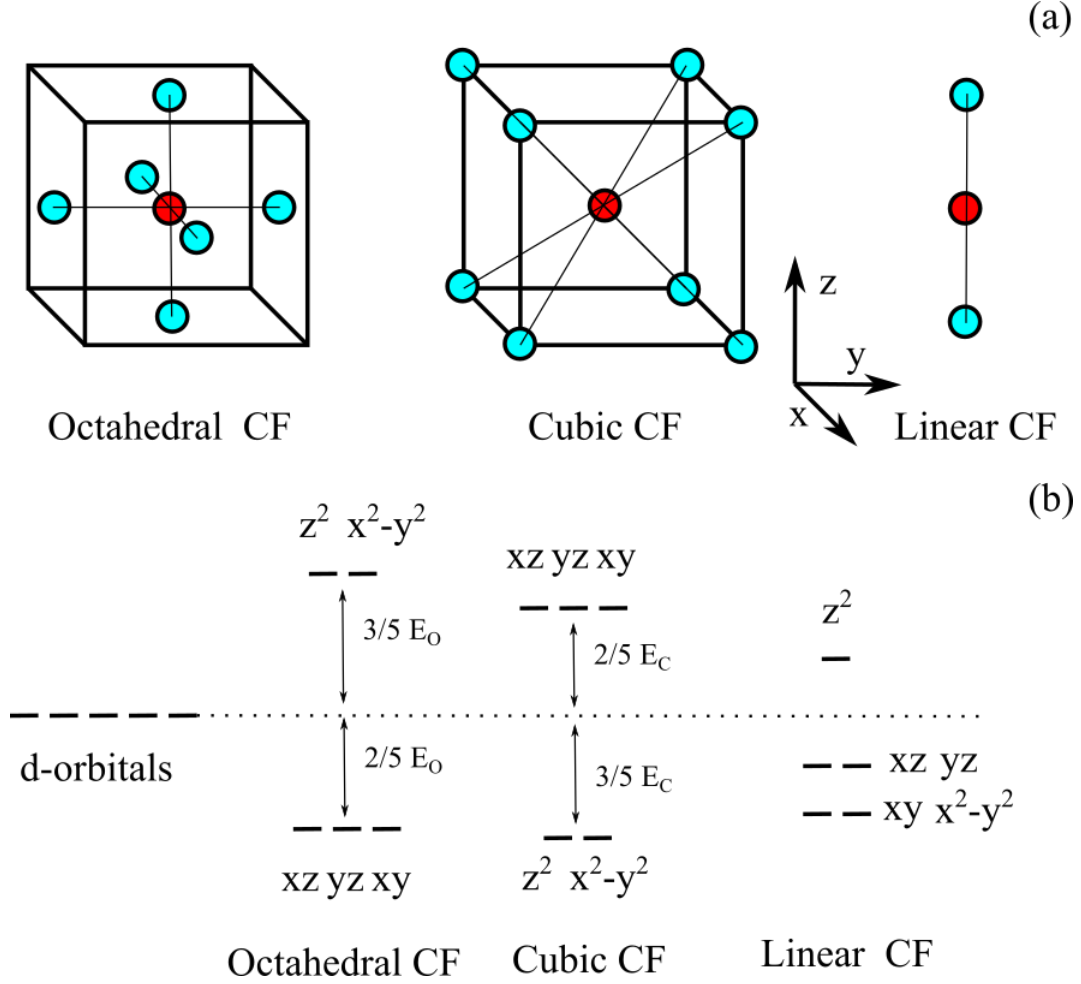


Figure 1. Illustration of crystal field splitting in transition metal oxides. Section (a) demonstrates structural diagrams of octahedral, cubic and linear crystal fields (CFs), with the transition metal atom marked in red and the ligand atom marked in cyan. Section (b) plots the energy splittings of d orbitals generated under these crystal fields.

are non-zero and add constructively to one another. From rule *R1*, for these two SHE contributions to be non-zero, we would require the d_{xz} & d_{yz} bands, as well as, the d_{xy} and $d_{x^2-y^2}$ bands to cross one another or be close enough in energy to enable SOC to mix them. The splitting of two d bands by crystal field into separate manifolds will hamper the mixing of those two bands. As such, the first principle to obtain large values of SHE (*C1*) is that the crystal field should be weak. For instance, in a weak octahedral or cubic crystal field, the e_g and t_{2g} manifolds overlap allowing band crossings between the d_{xy} and $d_{x^2-y^2}$ orbitals.

In materials with strong crystal fields, mixing between otherwise separate manifolds can be enhanced if structural distortions are present. Structural distortions of octahedral crystal

fields, such as octahedral rotation and tilting, have been shown to break up the e_g and t_{2g} manifolds into further sub-bands for SrIrO_3 [44]. This splitting up of a manifold increases the total bandwidth of that manifold, which encourages overlaps or transitions between separate manifolds. We would thus expect the presence of structural distortions to mitigate the dampening effect of a strong crystal field on SHE, and generate large SHE values. We call this condition of **structural distortions, condition 2 (C2)**. The enhancement of SHE via distortions has been experimentally reported for SrIrO_3 [34]. Although, we have derived conditions 1 and 2 (C1 & C2) specifically for octahedral crystal fields, they are general conditions extending beyond octahedral or even cubic crystal fields. This is because, in general, the weaker the crystal field, and the greater the structural distortions, the greater the possibility of mixing between various d -orbitals. Condition 3 (C3) is the same as the general rule 2 (R2), i.e., the **optimal positioning of the Fermi level**.

To deduce condition 4 (C4), we only focus on the t_{2g} manifold of octahedral and cubic crystal fields, and the transitions therein between the d_{xz} and d_{yz} orbitals. The impact of SOC is known to split the t_{2g} manifold into a lower energy $J_{\text{eff}} = 3/2$ and a higher energy $J_{\text{eff}} = 1/2$ sub-manifold [64]. The electron wavefunctions for the states in these $J_{\text{eff}} = 3/2$ & $1/2$ sub-manifolds can be written as:

$$\begin{aligned}
|j_{\text{eff}} = 3/2, m_j = 3/2\rangle &= -\frac{1}{\sqrt{2}}d_{yz} \otimes |\uparrow\rangle - \frac{i}{\sqrt{2}}d_{xz} \otimes |\uparrow\rangle \\
|j_{\text{eff}} = 3/2, m_j = 1/2\rangle &= -\frac{1}{\sqrt{6}}d_{yz} \otimes |\downarrow\rangle - \frac{i}{\sqrt{6}}d_{xz} \otimes |\downarrow\rangle + \sqrt{\frac{2}{3}}d_{xy} \otimes |\uparrow\rangle \\
|j_{\text{eff}} = 3/2, m_j = -1/2\rangle &= \frac{1}{\sqrt{6}}d_{yz} \otimes |\uparrow\rangle - \frac{i}{\sqrt{6}}d_{xz} \otimes |\uparrow\rangle + \sqrt{\frac{2}{3}}d_{xy} \otimes |\downarrow\rangle \\
|j_{\text{eff}} = 3/2, m_j = -3/2\rangle &= \frac{1}{\sqrt{2}}d_{yz} \otimes |\downarrow\rangle - \frac{i}{\sqrt{2}}d_{xz} \otimes |\downarrow\rangle
\end{aligned} \tag{12}$$

$$\begin{aligned}
|j_{\text{eff}} = 1/2, m_j = 1/2\rangle &= \frac{1}{\sqrt{3}}d_{yz} \otimes |\downarrow\rangle + \frac{i}{\sqrt{3}}d_{xz} \otimes |\downarrow\rangle + \sqrt{\frac{1}{3}}d_{xy} \otimes |\uparrow\rangle \\
|j_{\text{eff}} = 1/2, m_j = -1/2\rangle &= \frac{1}{\sqrt{3}}d_{yz} \otimes |\uparrow\rangle - \frac{i}{\sqrt{3}}d_{xz} \otimes |\uparrow\rangle - \sqrt{\frac{1}{3}}d_{xy} \otimes |\downarrow\rangle
\end{aligned} \tag{13}$$

where $|\uparrow\rangle$ & $|\downarrow\rangle$ are spin up and spin down states, respectively. In octahedral and cubic crystal fields, before the action of SOC, if the d_{xz} and d_{yz} orbitals are exactly degenerate, the electron wavefunctions will have exactly symmetric contributions from these two orbitals. Once SOC is turned on, in the absence of any mixing between the $J_{\text{eff}} = 3/2$ & $1/2$ states, the spin orbit coupled wavefunctions, given by eqs. 12, 13, will also have exactly symmetric

contributions from d_{xz} and d_{yz} orbitals. In such a case, the action of SOC would not lead to any $d_{xz}-d_{yz}$ transitions, and no resulting contribution to SHC (refer to rule *R3*). The reverse condition, i.e., octahedral and cubic crystal fields with degenerate d_{xz} and d_{yz} orbitals along with a mixing of $J_{\text{eff}} = 3/2$ & $1/2$ states could result in enhanced SHE values. We call this **condition 4 (C4)**. It is interesting to note that one way to enhance the mixing of $J_{\text{eff}} = 3/2$ & $1/2$ sub-manifolds is via structural distortions [44], thereby enhancing $d_{xz}-d_{yz}$ transitions. However, under CFT, structural distortions can themselves break the degeneracy between d_{xz} and d_{yz} orbitals, also generating $d_{xz}-d_{yz}$ transitions. Whether the two effects cooperate or cancel is not immediately obvious and would likely depend on the band structure details. Finally, **condition 5 (C5)** is that the presence of **moderate electron correlation** can enhance SHE by localizing electrons, as has been discussed in literature [45]. However, later we show that this effect is nuanced and depends on band structure details.

To summarize the five general rational design principles for large SHE are:

C1. Weak crystal fields.

C2. Structural distortions.

C3. Optimal positioning of the Fermi level.

C4. Mixing of $J_{\text{eff}} = 1/2$ & $3/2$ bands, for degenerate d_{xz} and d_{yz} orbitals, under octahedral or cubic crystal fields.

C5. Moderate electron correlations.

In the remaining sections, we report our findings on SHE in various *5d*-TMOs and explain them on the basis of these five rational design principles.

C. The effect of weak crystal field (C1)

We first report the finding of giant SHE in BCC-Pt₃O₄. Pt₃O₄ has two possible proposed crystal structures [65], body centered cubic (BCC) [66] and simple cubic (SC) [67]. BCC-Pt₃O₄ consists of Pt atoms surrounded by a cubic oxygen crystal field, while SC-Pt₃O₄ has Pt atoms inside a square planar crystal field. As we show below, the crystal field in BCC-Pt₃O₄ is weak which satisfies condition *C1*, leading to a giant SHE. The calculated spin Hall conductivity (SHC) for BCC-Pt₃O₄ is $3.7 \times 10^3 \hbar/2e \text{ S/cm}$ with an estimated giant spin Hall angle Θ_{SH} of ~ 7.4 . In sharp contrast to BCC-Pt₃O₄, SC-Pt₃O₄ displays a small SHC as a result of its strong crystal field which violates condition *C1*. Another exciting

result is the finding of a hypothetically giant SHE in the rare earth anti-perovskite Yb_3PbO . Yb_3PbO has Yb in a weak crystal field, satisfying condition *C1*. However, unfortunately, the nominal Fermi level in Yb_3PbO is poorly placed which violates condition *C3*. Engineering the Fermi level to place it at 0.6 eV above the nominal Fermi level of Yb_3PbO satisfies the condition *C3*, leading to an SHC of $-2.4 \times 10^3 \hbar/2e S/cm$ with an estimated giant Θ_{SH} of -2.5 to -4.9 . Though hypothetical, this latter result, alerts us to the possibility of finding giant SHE in *5d*-transition metal anti-perovskites via careful engineering of the Fermi level. Our preliminary results for SHE in TM_3PbO , where Yb atoms have been substituted by *5d*-transition metal (TM) atoms Hf and Ta, show promise towards achieving giant SHE in anti-perovskites. We will report these results in detail, in future work. The giant values of Θ_{SH} described in this section (and in Table I), are at least an order of magnitude larger than those reported for any TMOs so far. Additionally, these values are greater than those observed for all other measured materials except for $\text{Bi}_x\text{Se}_{1-x}$ and $\text{Bi}_{1-x}\text{Sb}_x$. Our spin Hall results give further support to the rational design principles deduced above.

$\text{BCC-Pt}_3\text{O}_4$ has a cubic crystal field which splits the *5d*-bands into a lower energy e_g and a higher energy t_{2g} manifold. A large Pt-O bond length of 2.7 Å leads to a weak crystal field (*C1*), which is evident from a significant overlap between the d_{xy} orbitals of the e_g manifold and the $d_{x^2-y^2}$ orbitals of the t_{2g} manifold, as seen in Fig. 2A:b,c. This overlap allows for multiple band crossings between the lower $d_{x^2-y^2}$ and the upper d_{xy} bands, along Γ -X as well as Γ -R in k-space, at E_F . Additionally, d_{xz} and d_{yz} bands also demonstrate various band crossings in this k-space region (see Fig. 2A:e). Turning on SOC leads to a clear mixing of these bands and a splitting of degeneracies (see Fig. 2A:c,f), creating spin orbit coupled states. This band mixing generates large spin Berry curvature along Γ -X and Γ -R, as shown in Fig. 2A:d, which results in a giant SHC. Note that the Fermi level is well-positioned as it passes through the region of band mixing. On the other hand, $\text{SC-Pt}_3\text{O}_4$ has Pt in a strong square planar crystal field, which violates condition *C1* leading to a significantly lower estimated Θ_{SH} of 0.5. A square planar crystal field splits the *5d*-bands into multiple manifolds, starting from a higher energy $d_{x^2-y^2}$ level, followed by d_{xy} and even lower d_{z^2} levels, and ending with the lowest energy level comprised of degenerate d_{xz} and d_{yz} bands. The strength of the square planar crystal field in $\text{SC-Pt}_3\text{O}_4$ is evident from the insignificant overlap between the d_{xy} and $d_{x^2-y^2}$ orbitals, as shown in Fig. 2B:b. Additionally, in the absence of SOC, we observe a minimal presence of d_{xz} and d_{yz} bands at the Fermi level, all

of which leads to a much smaller SHC than that seen for BCC-Pt₃O₄.

Yb₃PbO is an anti-perovskite, where the A and B sites of a regular perovskite have been swapped such that the central atom (Yb) is on the A site and Pb is on the B site. Every Yb atom is bonded to only two oxygen atoms with an O-Yb-O bond angle of 180°, constituting a linear ligand crystal field. Comprising only two ligand atoms makes the linear crystal field weak, satisfying condition C1 and allowing for a large SHE. This crystal field splits the *5d* bands into smaller manifolds, comprising degenerate d_{xz} and d_{yz} bands, and separately degenerate d_{xy} and $d_{x^2-y^2}$ bands. The weakness of this linear crystal field is evident from the overlap between these manifolds as shown in Fig. 2C:b,e. The degeneracy between d_{xy} and $d_{x^2-y^2}$ orbitals is further broken by a weak repulsion of the Yb- d_{xy} orbitals from the B site Pb ions (see Fig. 2C:a) that pushes the d_{xy} bands higher in energy (see Fig. 2C:b). The concerted effort of the weak ligand crystal field (condition C1), and a weak repulsive field from the cation Pb (modified condition C1), along with a hypothetical increase in the Fermi level by 0.6 eV (condition C3), leads to a giant SHE. At 0.6 eV above E_F , close to the *M* point, there is a band crossing between the lower Yb- $d_{x^2-y^2}$ bands and the upper Yb- d_{xy} bands, along with the presence of d_{xz} & d_{yz} orbitals (see Fig. 2C:b, e). SOC is expected to mix these bands and create a large hot spot for spin Berry curvature around *M*, which is shown in Fig. 2C:d. As a result, we see a giant estimated SH angle in Yb₃PbO for a Fermi level positioning of 0.6 eV above the nominal value. Yb₃PbO is identified as a possible topological crystalline insulator [52] with a Dirac node at the E_F [53], however we do not see any significant SHE contribution from this node.

Here we would like to note that while technically Yb₃PbO is a rare-earth oxide and not a TMO, a Fermi level which is 0.6 eV above the nominal Fermi level of Yb₃PbO passes through the empty *5d* bands of Yb, which brings our design principles into effect. As mentioned before, the optimal positioning of the Fermi level in anti-perovskites for giant SHE, can be achieved by substituting Yb atoms with the 5d-transition metal atoms Hf and Ta, such that the Fermi level passes through the *5d* bands. We also note that there exist many known 5d-transition metal anti-perovskite compounds (beyond oxides) such as Pt₃REB (RE: Rare Earth) [54], Pt₃AP (A = Sr, Ca, La) [57], while many more are theoretically predicted to be stable [58] and remain to be synthesized. Our preliminary calculations on these transition metal anti-perovskites show that giant spin Hall values can be obtained in anti-perovskites by careful engineering of the materials' chemical composition. We will report these results

Table I: List of SHC $\sigma_{\alpha\beta}^s$ ($\hbar/2eS/cm$), longitudinal conductivity σ and spin Hall angle $\Theta_{\alpha\beta}^s$			
Structure	$\sigma_{xy}^z = \sigma_{yz}^x = \sigma_{zx}^y$	σ (S/cm)	$\Theta_{xy}^z = \Theta_{yz}^x = \Theta_{zx}^y$
Experimental spin Hall values from literature for comparison			
β -W [29]	1000	3.3×10^3	0.3
Bi _{1-x} Sb _x [22]	1.3×10^5	2.5×10^3	52
SrIrO ₃ [34]	1300	2.5×10^3	0.5
IrO ₂ [24]	-	5.0×10^3	0.04
Prediction of giant spin Hall effect			
Pt ₃ O ₄ (BCC)	3676	$\sim 5 \times 10^2$ [55]	~ 7.4
Pt ₃ O ₄ (Cubic)	244	$\sim 5 \times 10^2$ [55]	~ 0.5
Yb ₃ PbO (E_F)	-124	$\sim 5 \times 10^2 - 10^3$ [56]	~ -0.1 to -0.3
Yb ₃ PbO ($E_F + 0.6$ eV)	-2448	$\sim 5 \times 10^2 - 10^3$ [56]	~ -2.5 to -4.9

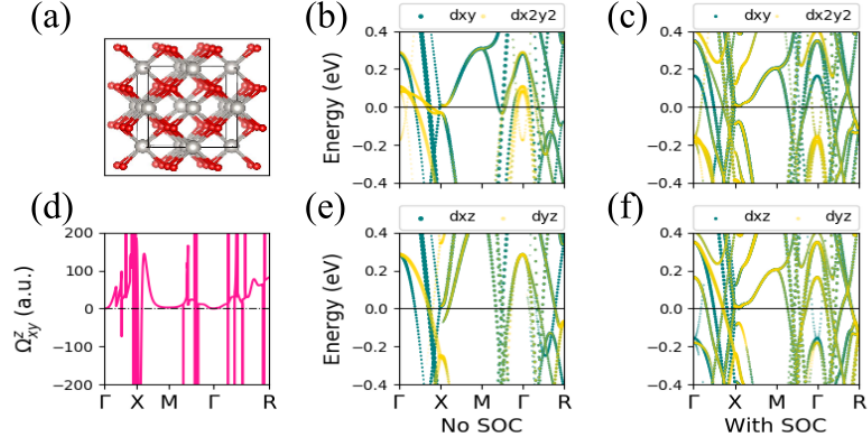
in detail in future work.

D. The role of structural distortions (C2)

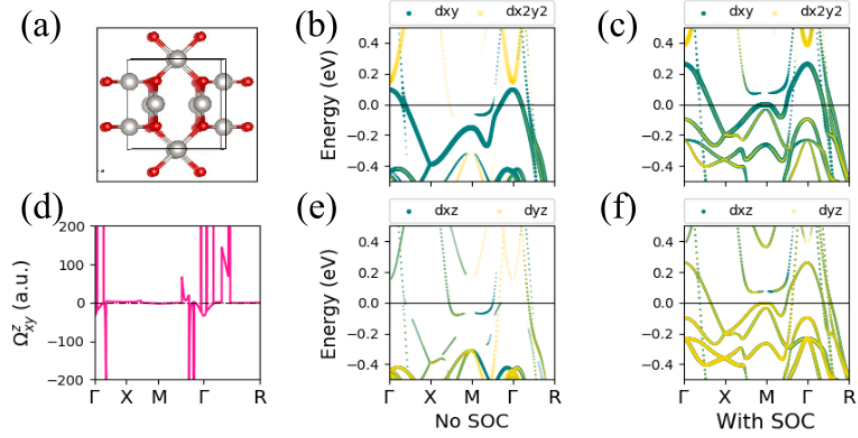
We now examine cubic perovskites where the transition metal atom is under a typically strong, octahedral crystal field. BaOsO₃ [68, 69] and SrOsO₃ [69] are both perovskite osmates with different sizes of the A site cation. As a result, BaOsO₃ adopts a perfect perovskite structure free from distortions, and demonstrates a low SHC, on account of its strong crystal field violating condition 1 (C1). In contrast, SrOsO₃ demonstrates large octahedral distortions, satisfying condition 2 (C2), which leads to a larger SHC for SrOsO₃. To account for correlation effects in BaOsO₃ and SrOsO₃, we use an LDA+U scheme with $U = 2$ eV which is taken from [69]. Like SrOsO₃, SrIrO₃ [44] also demonstrates significant distortions of the O6 octahedra, which satisfies condition C2, imparting a larger SHC to SrIrO₃ than BaOsO₃. The enhancement of SHC by structural distortions has been experimentally shown for SrIrO₃ [34]. The values of SHC and Θ_{SH} for these materials are calculated along the pseudo-cubic axes and are enumerated in Table II. An analysis of SHE in the rutile binary oxides OsO₂ and IrO₂ is included in the supplementary.

BaOsO₃ is a distortion-free cubic perovskite, with a metallic conductivity [68, 69], and an

A: BCC Pt₃O₄



B: Cubic Pt₃O₄



C: Yb₃PbO

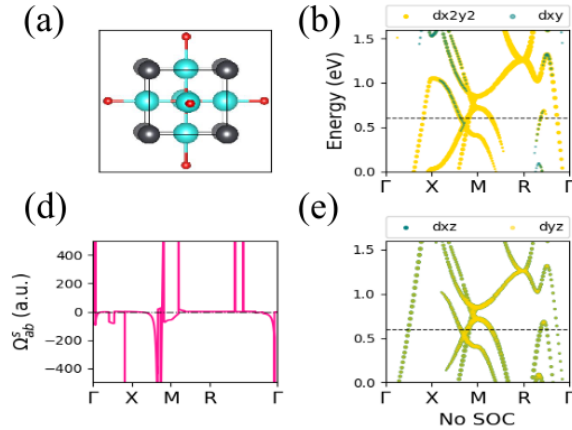


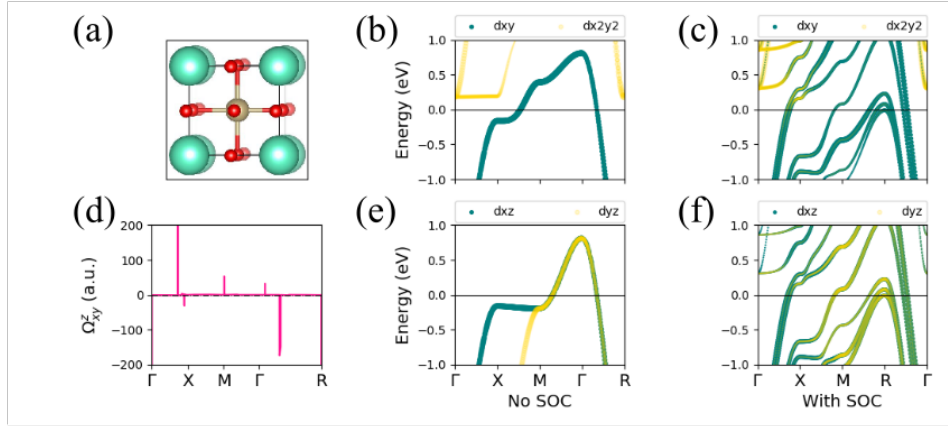
Figure 2. SHE in BCC-Pt₃O₄ (panel A), SC-Pt₃O₄ (panel B) and Yb₃PbO (panel C). Section (a) displays the structure of these oxides with Pt in silver, Yb in cyan, Pb in dark gray and O in red, (b) & (c) show the bandstructure projected onto d_{xy} orbitals (green) and $d_{x^2-y^2}$ orbitals (yellow), without and with SOC, respectively, (e) & (f) plot the bandstructure projected onto d_{xz} orbitals (green) and d_{yz} orbitals (yellow), without and with SOC, respectively, and (d) portrays the spin Berry curvature.

octahedral crystal field that splits the $5d$ -bands into a lower t_{2g} and an upper e_g manifold, with the Fermi level lying inside the former. The strong crystal field precludes any $e_g - t_{2g}$ overlap, violating condition $C1$, as is evident from Fig. 3A:b and resulting in a small SHC (see Table II).

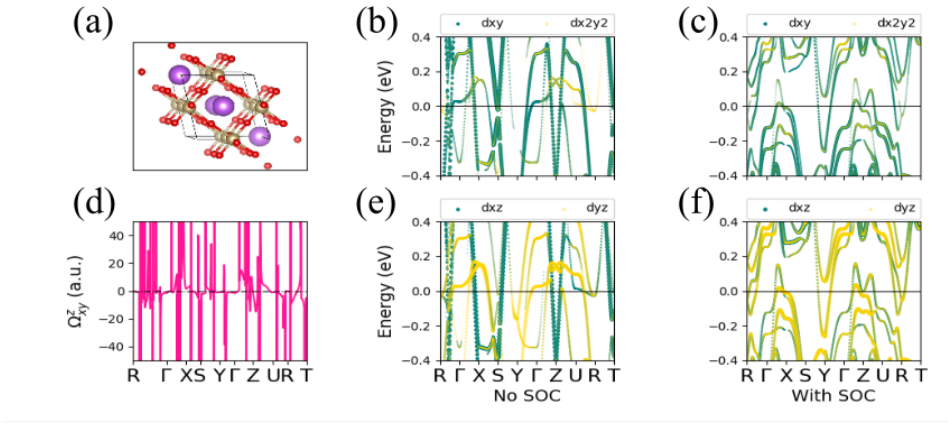
SrOsO_3 [69] and SrIrO_3 [44] are orthorhombic perovskites with a strong octahedral crystal field ($C1$), as well as the presence of structural distortions ($C2$). If acting alone, a strong crystal field violates condition $C1$, leading to a low SHC, as seen in BaOsO_3 . However, structural distortions satisfy condition $C2$ and mitigate the effect of crystal field, resulting in a larger SHC for SrOsO_3 and SrIrO_3 (see Table II). The mechanism by which structural distortions enhance SHE is evident from a comparison of the projected bandstructures for BaOsO_3 (see Fig. 3A: b,c), with that for SrOsO_3 (see Fig. 3B: b,c), or SrIrO_3 (see Fig. 3C: b,c). Distortions split the t_{2g} and e_g manifolds into multiple sub-bands, increasing the energy-span of both manifolds. This splitting, in turn, increases the likelihood of crossings between different sub-bands within a manifold, as well as crossings between different manifolds. This mechanism underpins condition $C2$. Although it has been shown for SrIrO_3 [44] that distortions also enhance the mixing of $J_{\text{eff}} = 1/2, 3/2$ states, whether this mixing contributes to SHE is difficult to ascertain, as distortions simultaneously break the degeneracy between d_{xz} and d_{yz} orbitals. Therefore, we are unsure if condition $C4$ applies.

The busy plots of band structure and spin Berry curvature for SrOsO_3 (see Fig. 3B: b-f) and SrIrO_3 (see Fig. 3C: b-f) make it difficult to isolate the exact regions of spin Hall generation. However, a broad inspection reveals multiple degeneracy splittings by the action of SOC. Inspection of projected band structures without SOC at the Fermi level reveals the presence of $e_g - t_{2g}$ overlap that is greater than that seen in BaOsO_3 . The $e_g - t_{2g}$ manifold overlap is greater for SrIrO_3 than SrOsO_3 owing to the increased band filling of the former. This overlap likely explains the order of SHC values seen which are largest for SrIrO_3 , followed by SrOsO_3 and smallest for BaOsO_3 . Our estimated values of Θ_{SH} for SrIrO_3 are $\Theta_{xy}^z \sim 0.2$ & $\Theta_{yz}^x \sim 0.34$ (see Table II) which are comparable to the experimentally observed values of $\Theta_{xy}^z \sim 0.5$ & $\Theta_{yz}^x \sim 0.3$ [34].

A: BaOsO₃



B: SrOsO₃



C: SrIrO₃

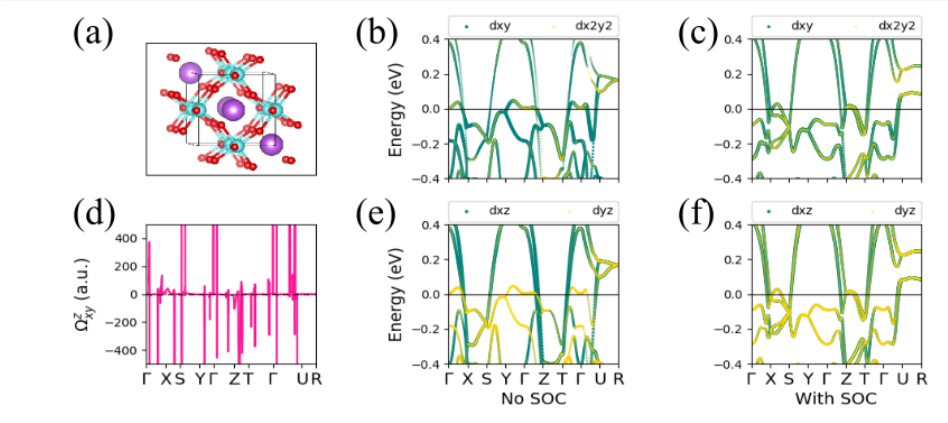


Figure 3. SHE in perovskite oxides including BaOsO₃ (panel A), SrOsO₃ (panel B) and SrIrO₃ (panel C). Section (a) displays the structure of these oxides with Os in yellow, Ba in green, Sr in purple, Ir in cyan and O in red, (b) & (c) show the bandstructure projected onto d_{xy} orbitals (green) and $d_{x^2-y^2}$ orbitals (yellow), without and with SOC, respectively, (e) & (f) plot the bandstructure projected onto d_{xz} orbitals (green) and d_{yz} orbitals (yellow), without and with SOC, respectively, and (d) portrays the spin Berry curvature. 16

Table II: List of SHC $\sigma_{\alpha\beta}^s$ ($\hbar/2e S/cm$), longitudinal conductivity σ and spin Hall angle $\Theta_{\alpha\beta}^s$							
Structure	σ_{xy}^z	σ_{yz}^x	σ_{zx}^y	σ (S/cm)	Θ_{xy}^z	Θ_{yz}^x	Θ_{zx}^y
Spin Hall predictions for cubic perovskites							
BaOsO ₃	-150	-134	-150	55 [85]	-2.7	-2.4	-2.7
SrOsO ₃	-294	30	276	128 [85]	-2.3	0.23	2.15
SrIrO ₃	382	680	84	2×10^3 [44]	0.2	0.34	0.05

E. The effect of electron correlations (*C5*)

In this section, we focus on the relationship between electron correlations and spin Hall effect captured in condition 5 (*C5*). It is generally expected that moderate electron correlations enhance SOC by localizing electrons [45], and should therefore enhance SHE as well. However, here we find that the effect of correlations on SHE is more nuanced and depends on band structure details (*C5*). While it is largely true that an increase in electron correlations increases the spin Berry curvature, the net effect of this enhancement on SHE can be complicated, due to the presence of competing spin Berry curvature hot spots, as well as local changes in band occupation caused by electron correlations.

Pyrochlore iridates, in particular rare-earth (RE) pyrochlore iridates, have generated keen interest for their interesting properties resulting from the interaction of moderate correlation and SOC [75]. These properties include the anomalous hall effect [76], spin-liquid state [77], Weyl semimetal [78, 79] etc. Here we study the SHE in a RE pyrochlore iridate, Tb₂Ir₂O₇ [70, 71]. In contrast, the pyrochlore iridate Bi₂Ir₂O₇ [72–74] has low electron correlations due to strong hybridization between Ir *5d* and Bi *6p* electrons [72]. We include electron correlations for Tb₂Ir₂O₇ under an LDA+U scheme with U ranging from 0 to 2.5 eV. Our results for SHE in Tb₂Ir₂O₇ and Bi₂Ir₂O₇ are listed in Table III, with the pyrochlore lattice vectors \vec{a} , \vec{b} & \vec{c} defined along $\hat{x} + \hat{y}$, $\hat{x} - \hat{y}$ & $\hat{x} + \hat{z}$ directions respectively. With increasing correlation (U), the SHC for Tb₂Ir₂O₇ shows non-linear, complex behaviour. For Bi₂Ir₂O₇ we predict a SHC of -122 to $-512 \hbar/2e S/cm$.

The complicated behaviour of SHC with correlations (U) observed in Tb₂Ir₂O₇, arises due to competing spin Berry curvature hot spots and changes in local band occupation caused by U. At the Fermi level, there exist two degeneracy points in the band structure of Tb₂Ir₂O₇

(see Fig. 4B: f), the first between L and Γ and the second between Γ and X . Turning on SOC breaks these degeneracies, opening up a gap and generating two spin Berry curvature hot spots (see Fig. 4B: a-e). These two hot spots give two separate contributions to the overall SHC. For σ_{xy}^z and σ_{yz}^x the two contributions to each usually oppose one another, with the first, $L - \Gamma$ hot spot contribution being larger than the second, $\Gamma - X$ hot spot contribution. With increase in U , the first contribution generally increases and the second contribution initially increases then decreases (see Fig. 4B: a-e). Thus, we see σ_{xy}^z and σ_{yz}^x first fall with increase of U and then rise. However for σ_{zx}^y , the two contributions usually add together constructively to yield a negative σ_{zx}^y , that first rises in value and then falls. The actual picture is more nuanced, but this explanation captures the essential trend.

The behaviour of the hot spot contributions with U is a result of local band fillings. For the first hot spot ($L - \Gamma$) the band fillings remain essentially unchanged as U increases (see Fig. 4B: f). Therefore, in general, increasing U increases the SHC contribution from this hot spot. However, for the second hot spot ($\Gamma - X$) the band filling changes substantially for one of the bands as U increases. When U is small the Fermi level goes cleanly through the gap created by SOC, which should maximize the total Berry curvature contribution from this hot spot (see Fig. 4B: f). When U is increased, the lower band is pushed just above the Fermi level, thereby decreasing the SHC contribution. Therefore, the second hot spot contribution initially increases and then decreases with increasing U . Overall, moderate electron correlations tend to enhance SHE. However, correlations can also suppress SHE in cases where there exist competing spin Berry curvature hot spots or where correlations alter the local band occupation. These inferences are encapsulated in condition 5 (*C5*) of our rational design principles.

III. METHODS

We performed calculations using QUANTUM ESPRESSO [80], WANNIER90 [81] and our in-house code which calculates spin Hall conductivity from the output of the former two codes. Previously, we have successfully used this method for the prediction of spin Hall conductivity in lanthanides [31]. Density functional theory calculations were carried out using QUANTUM ESPRESSO in order to obtain the electronic ground states for our TMOs. Convergence of total energy was ensured for every material, which required a plane-wave

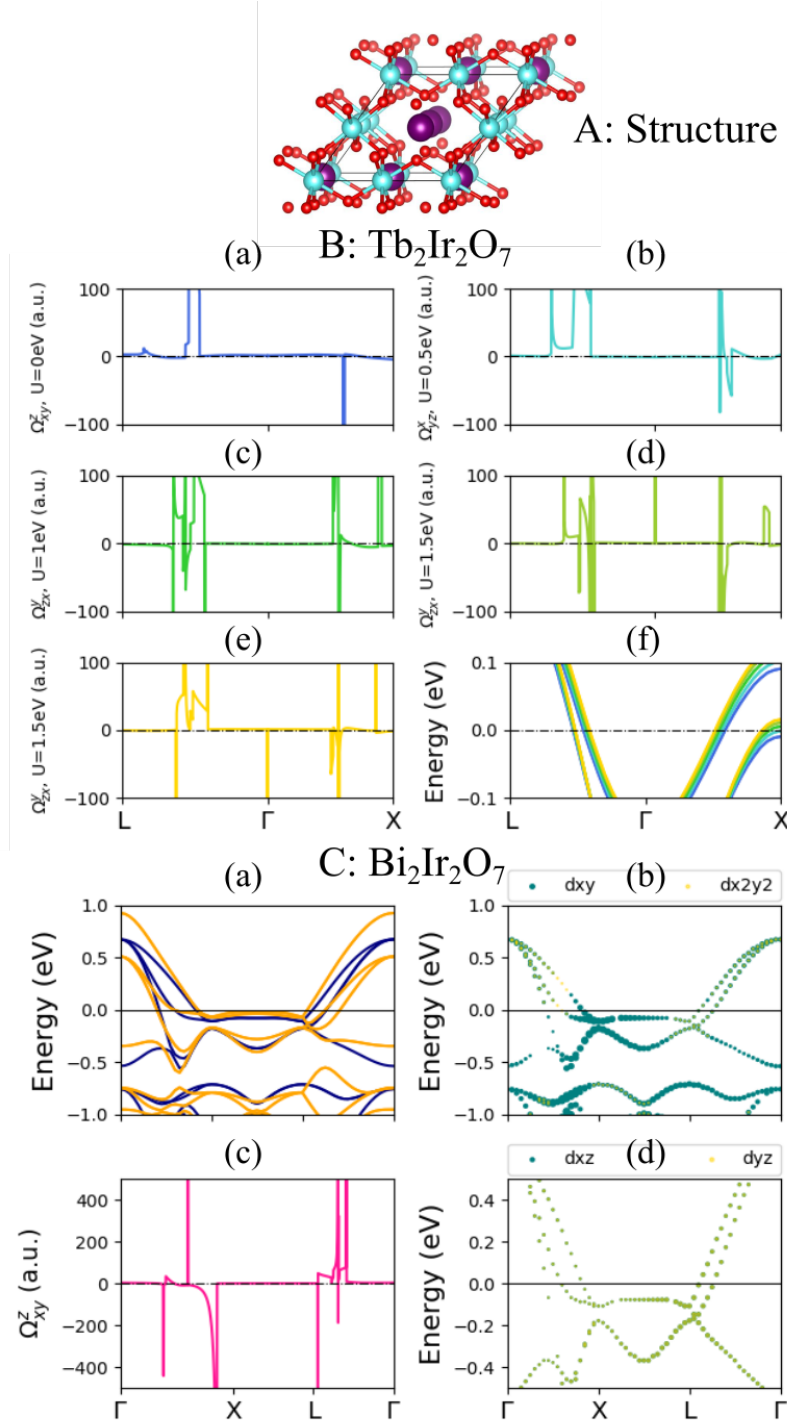


Figure 4. SHE in pyrochlore oxides including $\text{Tb}_2\text{Ir}_2\text{O}_7$ (panel B), $\text{Bi}_2\text{Ir}_2\text{O}_7$ (panel C). Panel A displays the structure with Tb/Bi in cyan, Ir in purple and O in red. For panel B, sections (a)-(e) display the spin Berry curvature plots for $\text{Tb}_2\text{Ir}_2\text{O}_7$ with correlation (U) values ranging from 0 to 1.5 eV and (f) portrays the bandstructure corresponding to the varying U values. For panel C, section (a) shows the bandstructure of $\text{Bi}_2\text{Ir}_2\text{O}_7$ without (blue) and with (orange) SOC, (b) displays the bandstructure projected onto d_{xy} orbitals (green) and $d_{x^2-y^2}$ orbitals (yellow) without SOC, (c) plots the spin Berry curvature and section (d) shows the bandstructure projected onto d_{xz} orbitals (green) and d_{yz} orbitals (yellow) without SOC.

Table III: List of SHC $\sigma_{\alpha\beta}^s$ ($\hbar/2e S/cm$), longitudinal conductivity σ and spin Hall angle $\Theta_{\alpha\beta}^s$							
Correlation	σ_{xy}^z	σ_{yz}^x	σ_{zx}^y	σ (S/cm)	Θ_{xy}^z	Θ_{yz}^x	Θ_{zx}^y
Spin Hall prediction for $\text{Tb}_2\text{Ir}_2\text{O}_7$							
U = 0.0 eV	-111	44	-142				
U = 0.5 eV	186	196	-188				
U = 1.0 eV	16	15	-527				
U = 1.5 eV	284	-10	-136				
U = 2.0 eV	-374	528	-56				
Spin Hall prediction for $\text{Bi}_2\text{Ir}_2\text{O}_7$							
U = 0.0 eV	-122	-512	-158	~ 714 [73]	-0.2	-0.7	-0.2

energy cut off between 160-200 Ry, and a k-mesh between 5x5x5 and 15x15x15, depending on the structure. Initial structures for these materials were taken from the following sources: BCC-Pt₃O₄ [66], SC-Pt₃O₄ [67], Yb₃PbO [84], BaOsO₃ [85], SrOsO₃ [85], SrIrO₃ [86], Tb₂Ir₂O₇ [70] and Bi₂Ir₂O₇ [72]. Structural optimization was subsequently performed to find the lowest energy structure.

We utilized norm-conserving, fully relativistic pseudopotentials in the local density approximation (LDA) [82, 83]. These pseudopotentials were constructed using the atomic pseudopotential engine [87] and were benchmarked against the fully relativistic all-electron potential. For an accurate estimation of SHC while using a k-mesh density small enough to be computationally viable, we mapped our DFT ground-state wave functions onto a maximally localized Wannier function basis using WANNIER90. Following this change of basis, we employed an adaptive k-mesh strategy inspired by [88] and employed our in-house code to extract the matrices relevant to the calculation of SHC. To analyze our results, we projected the bandstructures onto relevant atomic orbitals. For bandstructure calculations that included SOC, QUANTUM ESPRESSO did not give us the projection of orbital contributions onto the uncoupled spin orbital states. Therefore, for all materials except Yb₃PbO, we used Vienna Ab-initio Simulation Package (VASP)[89–91] as well as QUANTUM ESPRESSO to analyse the projected bandstructures. The projected bandstructures obtained from VASP were benchmarked with those generated by QUANTUM ESPRESSO for calculations without SOC. Due to difference in the pseudopotential cores for the rare-earth Yb atom, the

VASP and QUANTUM ESPRESSO projected bandstructures did not give the same results for Yb_3PbO . Here, we would like to note that often in the manuscript we have utilized modifiers to describe the strength of spin Hall angle, such as, giant, large etc. These terms are often vague and their meaning changes with every discovery. In this manuscript, we have used the term colossal to describe $\Theta_{\text{SH}} > 20$, giant for Θ_{SH} between 2 and 20 and large for Θ_{SH} between 0.2 and 2.0.

IV. SUPPLEMENTARY MATERIAL

A. Justification for neglecting the spin mixing contribution to SHE

Our rational design principles for large SHE have been derived under the assumption that in materials with inversion and time-reversal symmetry, the dominant contribution to SHE arises from the spin conserving part of the SOC ($\lambda \hat{l}_z \hat{s}_z$). This dominance of $\lambda \hat{l}_z \hat{s}_z$ has been observed in heavy metals like Pt [92]. Here we give an intuitive argument to show that this assumption is usually, though not always, valid. As shown in the main text, the anomalous velocity originating from the spin conserving part of SOC ($\lambda \hat{l}_z \hat{s}_z$) is \hat{v}_α^z for spin up and $-\hat{v}_\alpha^z$ for spin down. These two terms are always equal in value and opposite in sign, independent of the orbital character of the states. The contribution to spin Berry curvature originating in SOC, in particular the spin conserving part of SOC, is of the form $-\text{Im}[s_{nl}v_{\alpha,lm}^z v_{\beta,mn}^z]$, for say a spin up state. Then the corresponding term for the time reversed, spin down state would be $-\text{Im}[-(s_{nl})^* - (v_{\alpha,lm}^z)^* - (v_{\beta,mn}^z)^*]$. Using $\text{Im}(A^* B^* C^*) = -\text{Im}(ABC)$, we can show that these two terms will be equal and always add constructively.

In contrast, for the spin mixing part of SOC ($\lambda(\hat{l}_+ \hat{s}_- + \hat{l}_- \hat{s}_+)$), the anomalous velocity terms for spin up (\hat{v}_α^-) and spin down (\hat{v}_α^+) are not always exactly equal and opposite. Therefore, depending on the orbital character of the states, the contribution to SHC originating in these terms can interact constructively or destructively. When the contributions from these *spinmixing* terms interact destructively, it is the spin *conserving* part of SOC that gives the dominating term to SHC. Even when the spin *mixing* terms interact constructively, the spin *conserving* contribution can still be important.

B. Spin Hall effect in rutile binary oxides

Table SI: List of SHC $\sigma_{\alpha\beta}^s$ ($\hbar/2e$ S/cm), longitudinal conductivity σ and spin Hall angle $\Theta_{\alpha\beta}^s$							
Structure	σ_{xy}^z	σ_{yz}^x	σ_{zx}^y	σ (S/cm)	Θ_{xy}^z	Θ_{yz}^x	Θ_{zx}^y
Spin Hall predictions for rutile binary oxides							
OsO ₂	338	-1152	-950	1.7×10^4 [93]	0.02	-0.07	-0.07
IrO ₂	68	-288	-630	5.0×10^3 [94]	0.01	-0.06	-0.13

Similar to the cubic perovskites, rutile binary oxides such as OsO₂ [96, 97] and IrO₂ [97–99], also are composed of a transition metal atom inside an octahedral crystal field. This strong octahedral crystal field violates condition *C1*, however it displays a small orthorhombic distortion. To account for correlation effects in IrO₂, we use an LDA+U scheme with $U = 2$ eV which is taken from [98]. From our analysis below, it is likely that this distortion contributes to SHC via mixing of $J_{\text{eff}} = 1/2$ & $3/2$ states, satisfying condition *C5*. Together, these conditions result in a spin Hall conductivity of $\sim 10^2 - 10^3 \hbar/2e$ S/cm for OsO₂ and $\sim 10^2 \hbar/2e$ S/cm IrO₂. The values of SHC and Θ_{SH} for these materials are calculated along the pseudo-cubic axes and are enumerated in Table SI.

Acting alone, an octahedral crystal field is expected to split the *5d* bands into a lower energy t_{2g} , and a higher energy e_g manifold. The orthorhombic distortion breaks the degeneracy within the t_{2g} manifold by pushing the d_{xy} bands below the degenerate d_{xz} and d_{yz} bands (see Fig. 5A,B: b,d). The Fermi energy for both materials passes through the lower t_{2g} manifold, with IrO₂ having one more filled electron state per primitive unit cell than OsO₂. At the Fermi level, there exists a band crossing at the *Z* point in OsO₂ (see Fig. 5A: b,d) and close to the *Z* point, as well as in the *M* – *X* region, in IrO₂ (see Fig. 5B: b,d). These band crossings give rise to hot spots for spin Berry curvature (see Fig. 5A,B: c). To analyze the mechanism by which SHE is generated in these rutile oxides, we examine the projected bandstructures around the spin Berry curvature hot spot, as displayed in Fig. 5A,B: b,d. Around the hot spots, bands for both materials have a strong presence of d_{xz} and d_{yz} orbitals, suggesting that SHE arises primarily from $d_{xz} - d_{yz}$ transitions. The

orthorhombic distortions are expected to mix the $J_{\text{eff}} = 1/2, 3/2$ states [98], which satisfies condition $C4$, and has the effect of enhancing $d_{xz} - d_{yz}$ transitions. A small mixing of these J_{eff} states has been shown to occur for IrO_2 [98].

Recently, a study of SHE in IrO_2 [95] has found Dirac nodal lines (DNLs) [100, 101] to contribute towards SHE. For IrO_2 , a Dirac nodal line (DNL) is shown to occur in the segment of the band that extends in the $M - X$ region at E_F . Our findings of a spin Berry curvature hot spot in the $M - X$ region corroborates the results of [95]. It is interesting to note that DNLs have a direct relationship with SHC, as shown by the authors of [95]. Dirac nodal lines consist of a line of nodes, where each node is a topological singularity, such that an integral of the Berry curvature over a loop containing a Dirac node is equal to π [100, 101]. At points of crossing between bands of differing orbital character, SOC can mix these bands and create spin Berry curvature hot spots that are also Dirac nodes. In such cases, DNLs are essentially a series of spin Berry curvature hot spots that contribute to SHE, as shown for IrO_2 [95]. An interesting consequence of this relationship is that our rational design principles for large SHE can also be applied to encourage the formation of Dirac nodal lines in TMOs.

C. Spin Hall effect in other *5d* TMOs

We also list our predictions for SHE in other TMOs in Table SII. Initial structures for the TMOs included in the supplementary were taken from the following sources: OsO_2 [96], IrO_2 [102], WO_2 [103], NaWO_3 [104], ReO_3 [105], ReBiO_4 [106], $\text{Cd}_2\text{Re}_2\text{O}_7$ [107], CdPt_3O_6 [108], NaPt_3O_4 [109] and PbPt_2O_4 [110].

V. ACKNOWLEDGMENTS

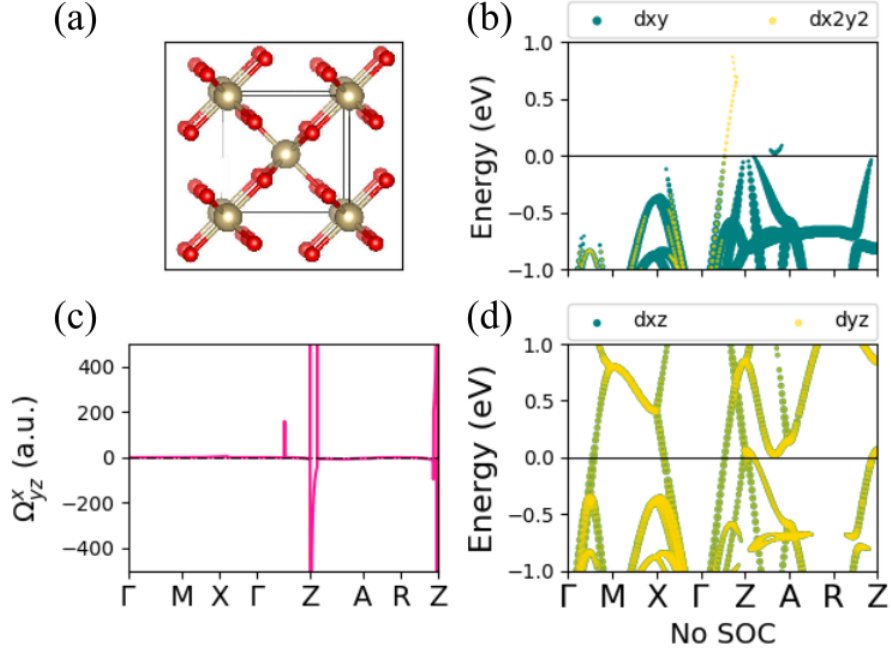
The authors would like to thank Dan Ralph for useful discussions and NSF for financial support under the grants NNCI ECCS-1542159, EFRI-newLAW and NASCENT ERC. They also acknowledge the Texas Advanced Computing Center (TACC) at The University of Texas at Austin for providing HPC resources that have contributed to the research results reported

Table SII: List of spin Hall conductivity $\sigma_{\alpha\beta}^s$ ($\hbar/2e \cdot S/cm$)			
Structure	σ_{xy}^z	σ_{yz}^x	σ_{zx}^y
WO ₂	-2	-120	78
NaWO ₃	-96	-126	-126
ReO ₃	-150	-150	-128
ReBiO ₄	-168	-78	182
Cd ₂ Re ₂ O ₇	-358	-374	-236
CdPt ₃ O ₆	-28	-58	-66
NaPt ₃ O ₄	204	360	300
PbPt ₂ O ₄	-12	284	-52

within this paper. URL: <http://www.tacc.utexas.edu>

-
- [1] Sander, D. et al. The 2017 magnetism roadmap. *J. Phys. D: Appl. Phys.* **50**, 363001 (2017).
 - [2] Tehrani, S. et al. Magnetoresistive random access memory using magnetic tunnel junctions. *Proc. IEEE* **91**, 703–714 (2003).
 - [3] Chappert, C., Fert, A. and Van Dau, F. N. The emergence of spin electronics in data storage. *Nat. Mater.* **6**, 813–823 (2007).
 - [4] Wolf, S. A. et al. Spintronics: a spin-based electronics vision for the future *Science* **294**, 1488–1495 (2001).
 - [5] Prinz, G. A. Magnetoelectronics. *Science* **282**, 1660–1663 (1998).
 - [6] Brataas, A., Kent, A. D. and Ohno, H. Current-induced torques in magnetic materials. *Nat. Mater.* **11**, 372–381 (2012).
 - [7] Otani, Y. Shiraishi, M. Oiwa, A. Saitoh, E. Murakami, S. Spin conversion on the nanoscale. *Nat. Phys.* **13**, 829–832 (2017).
 - [8] Gambardella, P. Miron, I. M. Current-induced spin-orbit torques. *Philos. Trans. A Math. Phys. Eng. Sci.* **369**, 3175–3197 (2011).
 - [9] Kuschel, T. and Reiss, G. Spin orbitronics: charges ride the spin wave. *Nat. Nanotechnol.* **10**, 22–24 (2015).

A: OsO₂



B: IrO₂

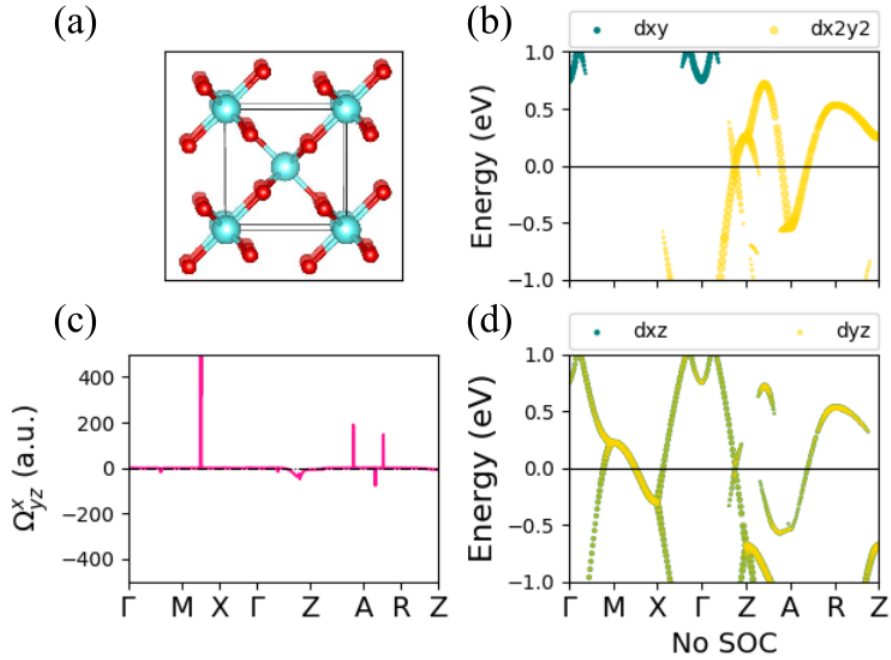


Figure 5. Analysis of SHE in rutile binary oxides, including OsO₂ (panel A) and IrO₂ (panel B). Section (a) displays the rutile structure of these oxides with Os in yellow, Ir in cyan and O in red, (b) shows the bandstructure projected onto d_{xy} orbitals (green) and $d_{x^2-y^2}$ orbitals (yellow), (c) portrays the spin Berry curvature and (d) plots the bandstructure projected onto d_{xz} orbitals (green) and d_{yz} orbitals (yellow).

- [10] Dyakonov, M. I. Perel, V. I. Current-induced spin orientation of electrons in semiconductors. *Phys. Lett. A* **35**, 459–460 (1971).
- [11] Hirsch, J. E. Spin Hall effect. *Phys. Rev. Lett.* **83**, 1834–1837 (1999).
- [12] Sinova, J. Valenzuela, S. O. Wunderlich, J. Back, C. H. Jungwirth, T. Spin Hall effects. *Rev. Mod. Phys.* **87**, 1213–1260 (2015).
- [13] Valenzuela, S. O. and Tinkham, M. Direct electronic measurement of the spin Hall effect. *Nature* **442**, 176–179 (2006).
- [14] Saitoh, E., Ueda, M., Miyajima, H. and Tatara, G. Conversion of spin current into charge current at room temperature: inverse spin-Hall effect. *Appl. Phys. Lett.* **88**, 182509 (2006).
- [15] Kimura, T., Otani, Y., Sato, T., Takahashi, S. and Maekawa, S. Room-temperature reversible spin Hall effect. *Phys. Rev. Lett.* **98**, 156601 (2007).
- [16] Edelstein, V. M. Spin polarization of conduction electrons induced by electric current in two-dimensional asymmetric electron systems. *Solid State Commun.* **73**, 233–235 (1990).
- [17] Rojas-Sanchez, J. C. et al. Spin-to-charge conversion using Rashba coupling at the interface between non-magnetic materials. *Nat. Commun.* **4**, 2944 (2013).
- [18] Isasa, M. et al. Origin of inverse Rashba-Edelstein effect detected at the Cu/Bi interface using lateral spin valves. *Phys. Rev. B* **93**, 014420 (2016).
- [19] Fan, Y. et al., Magnetization switching through giant spin-orbit torque in a magnetically doped topological insulator heterostructure. *Nat. Mater.* **13**, 699–704 (2014).
- [20] Rojas-Sanchez, J. C. et al., Spin to charge conversion at room temperature by spin pumping into a new type of topological insulator: α -Sn films. *Phys. Rev. Lett.* **116**, 096602 (2016).
- [21] Dankert, A., Geurs, J., Kamalakar, M. V., Charpentier, S. and Dash, S. P. Room temperature electrical detection of spin polarized currents in topological insulators. *Nano. Lett.* **15**, 7976–7981 (2015).
- [22] Khang, N. H. D. Ueda, Y. and Hai, P. N. A conductive topological insulator with large spin Hall effect for ultralow power spin-orbit torque switching. *Nat. Mater.* **17**, 808–813 (2018).
- [23] Mahendra, D. C. et al. Room-temperature perpendicular magnetization switching through giant spin-orbit torque from sputtered $\text{Bi}_x\text{Se}_{1-x}$ topological insulator material. *Nat. Mater.* **17**, 800–807 (2018).
- [24] Fujiwara, K. et al. 5d iridium oxide as a material for spin-current detection *Nat. Comm.* **4**, 2893 (2013).

- [25] Liu, L. Q. Moriyama, T. Ralph, D. C. Buhrman, R. A. Spin-Torque Ferromagnetic Resonance Induced by the Spin Hall Effect. *Phys. Rev. Lett.* **106**, 036601 (2011).
- [26] Kimura, T. Otani, Y. Sato, T. Takahashi, S. Maekawa, S. Room-Temperature Reversible Spin Hall Effect. *Phys. Rev. Lett.* **98**, 156601 (2007).
- [27] Ando, K. et al., Electric Manipulation of Spin Relaxation Using the Spin Hall Effect. *Phys. Rev. Lett.* **101**, 036601 (2008).
- [28] Mosendz, O. et al., Quantifying Spin Hall Angles from Spin Pumping: Experiments and Theory. *Phys. Rev. Lett.* **104**, 046601 (2010).
- [29] Pai, C.-F. et al. Spin transfer torque devices utilizing the giant spin Hall effect of tungsten. *Appl. Phys. Lett.* **101**, 122404 (2012).
- [30] Liu, L. et al. Spin-torque switching with the giant spin Hall effect of tantalum. *Science* **336**, 555–558 (2012).
- [31] Reynolds, N. et al. Spin Hall torques generated by rare-earth thin films. *Phys. Rev. B* **95**, 064412 (2017).
- [32] Mellnik, A. R. et al., Spin-transfer torque generated by a topological insulator. *Nature* **511**, 449–451 (2014).
- [33] Sahin, C. and Flatte, M. E. Tunable Giant Spin Hall Conductivities in a Strong Spin-Orbit Semimetal: $Bi_{1-x}Sb_x$ *Phys. Rev. Lett.* **114**, 107201 (2015).
- [34] Nan T. et al. Anisotropic spin-orbit torque generation in epitaxial $SrIrO_3$ by symmetry design. *PNAS* **116**, 16186–16191 (2019).
- [35] Ou et al. Exceptionally High, Strongly Temperature Dependent, Spin Hall Conductivity of $SrRuO_3$, *Nano Lett.* **19**, 3663–3670 (2019).
- [36] Hwang, H. Y. et al. Emergent phenomena at oxide interfaces. *Nat. Mater.* **11**, 103–113 (2012).
Imada, M., Fujimori, A. and Tokura, Y. Metal-insulator transitions. *Rev. Mod. Phys.* **70**, 1039–1263 (1998).
- [37] Vaz, D. C. Barthelemy, A. and Bibes, M. Oxide spin-orbitronics: New routes towards low power electrical control of magnetization in oxide heterostructures *Jpn. J. Appl. Phys.* **57**, 0902A4 (2018).
- [38] Kim, B. J. et al. Novel $J_{eff} = 1/2$ Mott State Induced by Relativistic Spin-Orbit Coupling in Sr_2IrO_4 . *Phys. Rev. Lett.* **101**, 076402 (2008).

- [39] Kim, B. J. et al. Phase-Sensitive Observation of a Spin-Orbital Mott State in Sr_2IrO_4 . *Science* **323**, 1329 (2009).
- [40] Liu et al. Direct observation of the Dirac nodes lifting in semimetallic perovskite $SrIrO_3$ thin films. *Sc. Rep.* **6**, 30309 (2016).
- [41] Biswas A., Kim, K.-S. and Jeong Y. H. Emergence of non-Fermi liquid behaviors in 5d perovskite $SrIrO_3$ thin films: Interplay between correlation, disorder, and spin-orbit coupling. *J. of Mag. and Mag. Mater.* **400**, 36–40 (2016).
- [42] Nie, Y. F. et al. Wan, X. Turner, A. M. Vishwanath, A. and Savrasov, S. Y. Topological semimetal and Fermi-arc surface states in the electronic structure of pyrochlore iridates. *Phys. Rev. B* **83**, 205101 (2011).
- [43] Chen, Y. Lu, Y.-M. and Hae-Young Kee, H.-Y. Topological crystalline metal in orthorhombic perovskite iridates. *Nat. Comm.* **6**, 6593 (2015).
- [44] Interplay of Spin-Orbit Interactions, Dimensionality, and Octahedral Rotations in Semimetallic $SrIrO_3$. *Phys. Rev. Lett.* **114**, 016401 (2015).
- [45] Witczak-Krempa, W. Chen, G. Kim, Y. B. and Balents, L. Correlated Quantum Phenomena in the Strong Spin-Orbit Regime, *Annu. Rev. Condens. Matter Phys.* **5**, 57-82 (2014).
- [46] Sun, Y. Zhang, Y. Liu, C.-X. Felser, C. and Yan, B. Dirac nodal lines and induced spin Hall effect in metallic rutile oxides *Phys. Rev. B* **95**, 235104 (2017).
- [47] Shao, D.-F. Gurung, G. Paudel, T. R. and Tsymbal, E. Y. Electrically reversible magnetization at the antiperovskite/perovskite interface. *Phys. Rev. Materials* **3**, 024405 (2019).
- [48] Sun, Y. et al. Negative Thermal Expansion and Magnetic Transition in Anti-Perovskite Structured $Mn_3Zn_{1-x}Sn_xN$ Compounds. *Journal of the American Ceramic Society* **93**, 2178 (2010).
- [49] Sun, Y. et al. Ni-doping effect on the magnetic transition and correlated lattice contraction in antiperovskite Mn_3ZnN compounds. *Solid State Commun.* **152**, 446 (2012).
- [50] Takenaka, K. Inagaki, T. and Takagi, H. Conversion of magnetic structure by slight dopants in geometrically frustrated antiperovskite Mn_3GaN . *Appl. Phys. Lett.* **95**, 132508 (2009).
- [51] Huang, R. et al. Spin-glass behavior in the antiperovskite manganese nitride Mn_3CuN codoped with Ge and Si. *Solid State Commun.* **150**, 1617-1620 (2010). Song, B. et al. Observation of spin-glass behavior in antiperovskite Mn_3GaN *Appl. Phys. Lett.* **92**, 192511 (2008).

- [52] Zhang, T. et al. Catalogue of topological electronic materials. *Nature* **566**, 475 (2019).
- [53] Pertsova, A. Geilhufe, R. M. Bremholm, M. and Balatsky, A. V. Computational search for Dirac and Weyl nodes in f-electron antiperovskites. *Phys. Rev. B* **99**, 205126 (2019).
- [54] Mondal, S. Mazumdar, C. Ranganathan, R. and Avdeev, M. Structural Transformation in Inverse-Perovskite $REPt_3B$ ($RE = \text{Sm}$ and Gd-Tm) Associated with Large Volume Reduction. *Inorg. Chem.* **56**, 8446–8453 (2017).
- [55] Neff, H. et al. Structural, optical, and electronic properties of magnetron-sputtered platinum oxide films. *J. App. Phys.* **79**, 7672 (1996).
- [56] Samal, D. Nakamura, H. and Takagi, H. Molecular beam epitaxy of three-dimensional Dirac material Sr_3PbO . *APL Mater.* **4**, 076101 (2016).
- [57] Chen, H. Xu, X. Cao, C. and Dai, J. First-principles calculations of the electronic and phonon properties of APt_3P ($A = \text{Ca}, \text{Sr}, \text{and La}$): Evidence for a charge-density-wave instability and a soft phonon. *Phys. Rev. B* **86**, 125116 (2012).
- [58] Bannikov, V. V. and Ivanovskii, A. L. Elastic and electronic properties of antiperovskite-type Pd- and Pt-based ternary carbides from first-principles calculations. *Journal of Alloys and Compounds* **577**, 615–621 (2013).
- [59] Murakami, S. Nagaosa, N. Zhang, S.-C. Dissipationless Quantum Spin Current at Room Temperature. *Science* **301**, 1348 (2003).
- [60] Sinova, J. et al. Universal Intrinsic Spin Hall Effect *Phys. Rev. Lett.* **92**, 126603 (2004).
- [61] Xiao, D. Chang, M.-C. Niu, Q. Berry phase effects on electronic properties. *Rev. Mod. Phys.* **82**, 1959 (2010).
- [62] Bethe, H. Termaufspaltung in Kristallen. *Annalen der Physik* **395**, 133–208 (1929).
- [63] Van Vleck, J. Theory of the Variations in Paramagnetic Anisotropy Among Different Salts of the Iron Group. *Physical Review* **41**, 208–215 (1932).
- [64] Stamokostas, G. L. and Fiete, G. A. Mixing of $t_{2g} - e_g$ orbitals in $4d$ and $5d$ transition metal oxides. *Phys. Rev. B* **97**, 085150 (2018).
- [65] Seriani, N. Pompe, W. and Ciacchi, L. C. Catalytic Oxidation Activity of Pt_3O_4 Surfaces and Thin Films. *J. Phys. Chem. B* **110**, 14860–14869 (2006).
- [66] Galloni, E. E. and Roffo, A. E. J. The Crystalline Structure of Pt_3O_4 *J. Chem. Phys.* **9**, 875 (1941).

- [67] Muller, O. and Roy, R. Formation and stability of the platinum and rhodium oxides at high oxygen pressures and the structures of Pt_3O_4 , $\beta\text{-PtO}_2$ and RhO_2 *J. Less-Common Metals* **16**, 129 (1968).
- [68] Jung, M.-C. and Lee, K.-W. Electronic structures, magnetism, and phonon spectra in the metallic cubic perovskite BaOsO_3 . *Phys. Rev. B* **90**, 045120 (2014).
- [69] Ali, Z. Sattar, A. Asadabadi, S. J. and Ahmad, I. Theoretical studies of the osmium based perovskites AOsO_3 ($A = \text{Ca, Sr and Ba}$). *J. Phys. Chem. Solids* **86**, 114–121 (2015).
- [70] Lefrancois, E. et al. Anisotropy-Tuned Magnetic Order in Pyrochlore Iridates. *Phys. Rev. Lett.* **114**, 247202 (2015).
- [71] Ishii, F. et al. First-Principles Study on Cubic Pyrochlore Iridates $\text{Y}_2\text{Ir}_2\text{O}_7$ and $\text{Pr}_2\text{Ir}_2\text{O}_7$. *J. Phys. Soc. Jap.* **84**, 073703 (2015).
- [72] Qi, T. F. Korneta, O. B. Wan, X. DeLong, L. E. Schlottmann, P. and Cao, G. Strong magnetic instability in correlated metallic $\text{Bi}_2\text{Ir}_2\text{O}_7$. *J. Phys.: Condens. Matter* **24**, 345601 (2012).
- [73] Lee, Y. S. et al. Infrared study of the electronic structure of the metallic pyrochlore iridate $\text{Bi}_2\text{Ir}_2\text{O}_7$. *Phys. Rev. B* **87**, 195143 (2013).
- [74] Wang, Q. Experimental electronic structure of the metallic pyrochlore iridate $\text{Bi}_2\text{Ir}_2\text{O}_7$. *J. Phys.: Condens. Matter* **27**, 015502 (2015).
- [75] Pesin, D. and Balents, L. Mott physics and band topology in materials with strong spin–orbit interaction. *Nat. Phys.* **6**, 376–381 (2010).
- [76] Machida, Y. Nakatsuji, S. Maeno, Y. Tayama, T. Sakakibara, T. and Onoda, S. Unconventional Anomalous Hall Effect Enhanced by a Noncoplanar Spin Texture in the Frustrated Kondo Lattice $\text{Pr}_2\text{Ir}_2\text{O}_7$. *Phys. Rev. Lett.* **98**, 057203 (2007).
- [77] Nakatsuji, S. et al. Metallic Spin-Liquid Behavior of the Geometrically Frustrated Kondo Lattice $\text{Pr}_2\text{Ir}_2\text{O}_7$. *Phys. Rev. Lett.* **96**, 087204 (2006)
- [78] Wan, X. Turner, A. M. Vishwanath, A. and Savrasov, S. Y. Topological semimetal and Fermi-arc surface states in the electronic structure of pyrochlore iridates. *Phys. Rev. B* **83**, 205101 (2011).
- [79] Witczak-Krempa, Go, W. A. and Kim, Y. B. Pyrochlore electrons under pressure, heat, and field: Shedding light on the iridates. *Phys. Rev. B* **87**, 155101 (2013).

- [80] Giannozzi, P. et al. QUANTUM ESPRESSO: a modular and open-source software project for quantum simulations of materials. *J. Phys.: Condens. Matter* **21**, 395502 (2009).
- [81] Mostofi, A. A. Yates, J. R. Lee, Y.-S. Souza, I. Vanderbilt, D. and Marzari, N. wannier90: A tool for obtaining maximally-localised Wannier functions *Comput. Phys. Commun.* **178**, 685 (2008).
- [82] Perdew, J. P. and Wang, Y. Accurate and simple analytic representation of the electron-gas correlation energy. *Phys. Rev. B* **45**, 13244 (1992).
- [83] Perdew, J. P. and Zunger, A. Self-interaction correction to density-functional approximations for many-electron systems. *Phys. Rev. B* **23**, 5048 (1981).
- [84] Persson, K. Materials Data on Yb₃PbO (SG:221) by Materials Project. (2014) DOI: 10.17188/1188128.
- [85] Shi, Y. et al. High-Pressure Synthesis of 5d Cubic Perovskite BaOsO₃ at 17 GPa: Ferromagnetic Evolution over 3d to 5d Series. *J. Am. Chem. Soc.* **135**, 16507-16516 (2013).
- [86] Zhao, J. G. et al. High-pressure synthesis of orthorhombic SrIrO₃ perovskite and its positive magnetoresistance. *J. App. Phys.* **103**, 103706 (2008).
- [87] Oliveira, M. J. T. and Nogueira, F. Generating relativistic pseudo-potentials with explicit incorporation of semi-core states using APE, the Atomic Pseudo-potentials Engine. *Comp. Phys. Comm.* **178**, 524-534 (2008).
- [88] Wang, X. Yates, J. R. Souza, I. and Vanderbilt, D. Ab initio calculation of the anomalous Hall conductivity by Wannier interpolation. *Phys. Rev. B* **74**, 195118 (2006).
- [89] Kresse, G. & Hafner, J. Ab initio molecular dynamics for liquid metals. *Physical Review B* **47**, 558 (1993).
- [90] Kresse, G. & Furthmüller, J. Efficiency of ab-initio total energy calculations for metals and semiconductors using a plane-wave basis set. *Computational materials science* **6**, 15-50 (1996).
- [91] Kresse, G. & Furthmüller, J. Efficient iterative schemes for ab initio total-energy calculations using a plane-wave basis set. *Physical review B* **54**, 11169 (1996).
- [92] Kontani, H. Naito, M. and Hirashima, D. S. Study of Intrinsic Spin and Orbital Hall Effects in Pt Based on a (6s, 6p, 5d) Tight-Binding Model. *J. Phys. Soc. Jpn.* **76**, 103702 (2007).
- [93] Rogers, D. B. Shannon, R. D. Sleight, A. W. and Gillson, J. L. Crystal chemistry of metal dioxides with rutile-related structures. *Inorg. Chem.* **8**, 841 (1969).

- [94] Fujiwara, K. et al. 5d iridium oxide as a material for spin-current detection. *Nat. Comm.* **4**, 2893 (2013).
- [95] Sun, Y. Zhang, Y. Liu, C.-X. Felser, C. and Yan, B. Dirac nodal lines and induced spin Hall effect in metallic rutile oxides *Phys. Rev. B* **95**, 235104 (2017).
- [96] Hayakawa, Y. et al. Electronic structure and electrical properties of amorphous OsO₂. *Phys. Rev. B* **59**, 125 (1999).
- [97] Mattheiss, L. F. Electronic structure of RuO₂, OsO₂, and IrO₂. *Phys. Rev. B* **13**, 2433 (1976).
- [98] Panda, S. K. Bhowal, S. Delin, A. Eriksson, O. and Dasgupta, I. Effect of spin orbit coupling and Hubbard U on the electronic structure of IrO₂. *Phys. Rev. B* **89**, 155102 (2014).
- [99] Ping, Y. Galli, G. and Goddard, W. A. Electronic Structure of IrO₂: The Role of the Metal d Orbitals. *J. Phys. Chem. C* **119**, 11570–11577 (2015).
- [100] Fang, C. Chen, Y. Kee, H.-Y. and Fu, L. Topological nodal line semimetals with and without spin-orbital coupling. *Phys. Rev. B* **92**, 081201(R) (2015).
- [101] Chen, Y. Kim, H.-Y. and Kee, H.-Y. Topological crystalline semimetals in nonsymmorphic lattices. *Phys. Rev. B* **93**, 155140 (2016).
- [102] Bolzan, A. A. Structural Studies of Rutile-Type Metal Dioxides. *Acta Cryst.* **B53**, 373-380 (1997).
- [103] Palmer, D. J. Tungsten Dioxide: Structure Refinement by Powder Neutron Diffraction. *Acta Cryst.* **B35**, 2199-2201 (1979).
- [104] Persson, K. Materials Data on NaWO₃ (SG:221) by Materials Project. (2014) DOI: 10.17188/1194248.
- [105] Myron, H. W. Gupta, R. P. and Liu, S. H. Study of the Electronic Structure of ReO₃ and its Pressure Dependence by the Korringa-Kohn-Rostoker Method. *Phys. Rev. B* **8**, 1292 (1973).
- [106] Persson, K. Materials Data on NaWO₃ (SG:221) by Materials Project. (2016) DOI: 10.17188/1201578.
- [107] Donohue, P. C. Longo, J. M. Rosenstein, R. D. and Katz, L. The Preparation and Structure of Cadmium Rhenium Oxide, Cd₂Re₂O₇. *Inorg. Chem.* **4**, 1152 (1965).
- [108] Prewitt, C. T. Schwartz, K. B. and Shannon, R. D. Synthesis and Structure of Orthorhombic Cadmium Platinum Oxide CdPt₃O₆. *Acta Cryst.* **C39**, 519-521 (1983).

- [109] Waser, J. and McClanahan, E. D. J. The Crystal Structure of NaPt_3O_4 . *J. Chem. Phys.* **19**, 413 (1951).
- [110] Tancret, N. Obbade, S. Bettahar, N. and Abraham, F. Synthesis and ab initio Structure Determination from Powder X-Ray Diffraction Data of a New Metallic Mixed-Valence Platinum–Lead Oxide PbPt_2O_4 . *J. Sol. Stat. Chem.* **124**, 309–318 (1996).